Tailoring the acidity of ZSM-5 via surface passivation: Catalytic assessment on dimethyl ether to olefins (DTO) process

Fuel 362 (2024) 130559

Contents lists available at ScienceDirect

Fuel

journal homepage: www.elsevier.com/locate/fuel

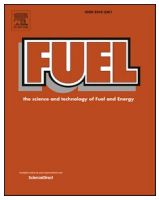

Full Length Article

Tailoring the acidity of ZSM-5 via surface passivation: Catalytic assessment on dimethyl ether to olefins (DTO) process

Emanuele Giglio [a,*], Giorgia Ferrarelli [a,b], Fabio Salomone [c], Elena Corrao [c], Massimo Migliori [a], Samir Bensaid [c], Raffaele Pirone [c], Girolamo Giordano [a]

[a] Chemical Engineering and Catalysis for Sustainable Processes (CECaSP) Laboratory, University of Calabria, Via Pietro Bucci, 87036 Rende, Italy
[b] Laboratory of Catalysis for Sustainable Production and Energy, University of Messina, Viale F. Stagno D'Alcontres 31, 98165 Messina, Italy
[c] Department of Applied Science and Technology (DISAT), Polytechnic of Turin, Corso Duca degli Abruzzi 24, 10129 Turin, Italy

ARTICLE INFO

Keywords:
Dimethyl ether conversion
Light olefins
Acid zeolites
Surface passivation
Core–shell
Deactivation

ABSTRACT

In the present study, four different samples having different acidity were synthesized. Two MFI-type zeolites having silicon-to-aluminum ratio equal to 25 and 50 were prepared. Besides, two additional samples were obtained by external passivation of each parent zeolite with a layer of Silicalite-1, leading to a core–shell structure. Each sample was characterized to assess textural properties, structure, composition, and acidity, and then tested for dimethyl ether (DME) conversion at different reaction temperatures between 300 and 375 °C. The analysis of produced mixture revealed the simultaneous presence of hydrocarbons and methanol. DME conversion grew by increasing the temperature. Propylene was the most abundant hydrocarbon detected during all the time-on-stream analyses. Especially at 375 °C, the investigated samples having greater acidity showed faster deactivation due to coking. Samples with lower acidity were thus more stable but, on the other hand, they presented higher methanol selectivity and lower hydrocarbons yield.

1. Introduction

Climate change caused by greenhouse gas emissions poses the need for an increasing exploitation of renewable energy sources (RES). In 2019, about 26 % of total world electricity was produced via RES including hydropower, solar, wind, geothermal, tide/wave/ocean, biofuels, and waste [1]. During the last decades renewable electricity generation showed a continuously increasing trend, passing from ≈ 1300 to ≈ 7000 TWh between 1973 and 2019 [1]. Worldwide electricity production from wind and solar in 2021 was equal to 1862 TWh and 1033 TWh, respectively, with an annual growth rate of 17.0 % (wind) and 22.3 % (solar) [2]. Renewables like photovoltaic and wind power generate electricity intermittently, posing challenges in terms of grid balance and management as their penetration in the energy systems increases.

Storage technologies are thus required to boost the share of RES in the energy mix of a country/region. Among the possible ways to convert and transform surplus renewable electricity, chemical storage can play an important role due to its potential capacity, in the framework of Power-to-X technologies. According to this pathway, electricity is converted into hydrogen via water/steam electrolysis. The produced hydrogen may react with captured carbon dioxide over appropriate catalysts and under suitable reaction conditions, leading to the production of synthetic fuels like methane [3–7], hydrocarbon mixtures [8–15], methanol [16–21] or dimethyl ether (DME) [22–24], depending on involved catalyst and operating condition. Methanol and DME can be converted into light olefins in presence of an acid catalyst according to methanol-to-olefins (MTO) and DME-to-olefins (DTO) process, respectively [25–28]. If methanol and DME were produced through the reaction between captured carbon dioxide and green hydrogen, olefins production would be carried out according to a sustainable pathway.

Light olefins like ethylene and propylene are key building-block components for the petrochemical industry. They are involved in plastics production (polyethylene, polypropylene) and in the synthesis of chemicals like ethylbenzene, acetaldehyde, vinyl acetate, acrylonitrile, cumene, acrylic acid alcohols (e.g., isopropanol), oxides (ethylene oxide and propylene oxide). The global demand in 2018 for ethylene and propylene was about 168 and 110 million tons, respectively [29,30]. Light olefins are conventionally produced via steam cracking of petroleum hydrocarbons.

* Corresponding author.
E-mail address: emanuele.giglio@unical.it (E. Giglio).

https://doi.org/10.1016/j.fuel.2023.130559
Received 7 September 2023; Received in revised form 18 November 2023; Accepted 3 December 2023

In the open literature great attention has been recently paid to the production of light olefins via catalytic dehydration of methanol and/or dimethyl ether. DME can be produced in a single- or two-stage process involving methanol dehydration as the last step. Olefins production from DME presents some advantages like higher reaction rates and hydrocarbons selectivity, reduced thermodynamic limitation and lower overall exothermicity of the process [31].

Exothermal dehydration of methanol into DME is considered as the first step in the reaction pathway towards olefins production, but the lower water amount leads to a greater conversion extent [32].

Several works available in the open literature deal with DTO focused on SAPO-type catalysts [33–35], since they have been widely employed for MTO process. Hirota et al. have investigated the effect of SAPO-34 crystal size in MTO and DTO [25], concluding that nanocrystals facilitate the diffusion of lighter products before they are converted into coke that may occlude the pores leading to fast deactivation. Micropores of SAPO-34 seems to favor the rapid deactivation during MTO/DTO; hierarchical structures with larger pores have been thus synthesized to obtain larger pores, leading to improved stability [36]. Lee et al. have studied as the use of binders like ZrO_2 with SAPO-34 improve the lifetime of catalysts. The addition of a binder seems to help the diffusion of the reactants and products between SAPO-34 crystals, while free SAPO-34 catalyst undergoes rapid deactivation due to the blockage of diffusion paths by coke species [37]. Deactivation kinetics based mechanistic investigation of coke formation over SAPO-34 during DTO has been proposed by Gao et al. [38]. Zhao et al. have studied the DME conversion over SAPO-18/34 intergrowth structures and the effect of phase composition [39,40]. Zhang et al. have focused on bead-milling and subsequent porogen-assisted recrystallization to generate nanocrystalline SAPO-34 that showed improved stability with respect to the parent sample [41]. DTO carried out with SAPO catalysts generally shows fast deactivation, high light olefins selectivity and superior ethylene/propylene ratio in the product stream with respect to other zeolite/zeotype structures [33,40].

Works focusing on MFI structure zeolites for DTO in the open literature usually involved commercial HZSM-5 [42–44]. Al-Dughaither and de Lasa tested HZSM-5 pellets (with alumina as binder and filler) having different silicon-to-aluminum ratio (Si/Al) [31]. Pérez-Uriarte et al. have focused on commercial HZSM-5 pellets in comparison with SAPO-type catalyst [45], with different SiO_2/Al_2O_3 ratio [46], at different temperature and space velocity [32]. A lumped kinetic model for DME conversion, as well as deactivation kinetics have been proposed [47,48]. Nano-sized hierarchical ZSM-5 zeolite prepared via a consecutive freezing and vacuum drying procedure showed improved stability and higher propylene content with respect to conventional ones [49]. The addition of promoters like La, Ca and Mg, to HZSM-5 has been also studied [50–52]. Other structures investigated in the open literature for DTO process are MCM-68 [53], MOR [54,55] and EU-1 [56–58].

In this work, MFI-type zeolites with relatively low Si/Al ratios have been prepared, thoroughly characterized, and tested for dimethyl ether conversion. The deposition of a Silicalite-1 layer passivating the external surface of a ZSM-5 zeolite (leading to a 'core-shell' structure) has been carried out, and its effect on catalytic conversion and stability has been investigated. Light olefins and by-products selectivity, coke formation and catalyst deactivation have been evaluated by varying the acidity of the samples and the reaction temperature.

2. Materials and methods

2.1. Catalysts synthesis and characterization

Two MFI-type zeolites with Si/Al ratio in the synthesis gel equal to 25 and 50 were synthesised according to the procedure described elsewhere [59]. The synthesis gels were prepared according to the following molar ratios:

$$Na_2O - 0.08\ TPABr - 1\ SiO_2 - x\ Al_2O_3 - 20\ H_2O$$

(where x = 0.01–0.02 to set the Si/Al ratio). The chemicals used for the syntheses were Silica gel 60 (Aldrich), sodium aluminate ($NaAlO_2$, Aldrich), sodium hydroxide (Aldrich), distilled water and tetrapropylammonium bromide (TPABr, VWR Chemicals) as structure directing agent (SDA). The hydrothermal syntheses were conducted in 150 ml PTFE-lined stainless-steel autoclave at 170 °C for 4 days (Si/Al ratio = 25) and for 3 days (Si/Al ratio = 50). The crystalline phase was separated from the mother liquor, carefully washed with distilled water, and dried at 90 °C overnight. A part of the synthetized zeolites was subjected to the classical procedure to obtain the H^+-form: a first calcination at 550 °C (heating rate 5 °C/min) for 8 h, two ion exchange cycles with NH_4Cl (1 M) and a second calcination at 550 °C. The obtained samples in H^+-form were named ZSM5_25 and ZSM5_50.

The remaining part of the as-made zeolites, without any calcination and ion exchange step, underwent through the surface-passivation procedure. The epitaxial growth of a Silicalite-1 thin layer was used as technique to neutralize the acid sites at the zeolite surface. To avoid the risk of a growing of Silicalite-1 that would partially obstruct the pores of ZSM-5 phase, altering its physical and acidic properties, in this work the as-made form of the ZSM-5 zeolites (i.e., with the pores still occupied by the SDA) was passivated [60]. Silicalite-1 synthesis gel was prepared using the following molar ratios:

$$SiO_2 - 0.5\ TPAOH - 8\ EtOH - 120\ H_2O$$

Tetraethyl orthosilicate (TEOS, VWR Chemicals), tetrapropylammonium hydroxide (TPAOH, Fluka Chemika), ethanol (EtOH, Carlo Erba) and deionized water were mixed and stirred for 1 h. Then, the as-made form of MFI crystals was mixed with the synthesis gel and transferred in a Teflon-lined stainless-steel autoclave. The hydrothermal synthesis was conducted at 180 °C for 24 h in a tumbling oven. Samples were washed with distillate water and dried at 90 °C overnight. The procedure was repeated twice, promoting the growth of a second layer of Sil-1 over the small crystals of Silicalite-1 deposited during the first synthesis. To get the H^+-form, passivated samples were calcined at 550 °C (heating rate: 2 °C/min), ion-exchanged twice with NH_4Cl (1 M) and then calcined again at 550 °C. Samples obtained after these steps were named PAS_25 and PAS_50 (where "PAS" indicates the passivation process and "25" or "50" the Si/Al ratio of the "core" ZSM-5 phase respectively).

X-ray Powder Diffraction (XRD) was used to confirm the crystalline structure of samples. Analyses was conducted using a Miniflex600 (Rigaku, Japan) in the 5-50° 2theta range. Atomic absorption spectroscopy (AAS) provided information about the chemical composition of the zeolites, particularly taking care of the aluminium and silicon content before and after the passivation cycles.

Sample morphology was studied through scanning electron microscopy (Phenom Pro G6, ThermoFisher Sci). SEM images were collected at different magnifications for all catalyst after gold coating. In order to estimate the Si/Al ratio, EDX analysis at 5, 10 and 15 kV were performed. EDX analysis performed at 5 kV were used to appreciate the difference between surface Si/Al ratios of the catalysts and to demonstrate the growth of Silicalite-1.

Textural properties such as BET surface area, micropore area, external surface area, were measured using N_2 adsorption/desorption isotherms at ≈ −196 °C (77 K) (ASAP2020, Micromeritics). To identify the quantity of Brønsted and Lewis acid sites, FT-IR analysis was performed using Nicolet iS 10 (Thermo Scientific, USA), equipped with a DTGS detector. The samples were compressed (under a load of 2.65 ton • cm^{-2}) into a wafer of about 25 mg and pre-treated at 400 °C in vacuum (about 10^{-5} torr). FT-IR spectra were recorded after deuterated acetonitrile (d_3-acetonitrile) chemisorption. Samples wafers were exposed to probe vapour pressure with a subsequent evacuation for 1 h at 25 °C. The Lambert-Beer law was used to evaluate the total number of acid sites

starting from the integrated area of the bands of the protonated species through the following equation:

$$A = \varepsilon \cdot N \cdot \rho \quad (1)$$

Where A is the area obtained from the spectra, ε is the molar extinction coefficient ($cm \cdot mmol^{-1}$), N is the concentration of the vibrating species ($mmol \cdot g^{-1}$), and ρ is the areal density of the disk ($mg \cdot cm^{-2}$). The value of molar extinction coefficients used were $\varepsilon = 2.05\ cm \cdot mmol^{-1}$for d_3-acetonitrile on Brønsted acid sites (BAS), band at ca. 2297 cm^{-1} and $\varepsilon = 3.6\ cm \cdot mmol^{-1}$ for d_3-acetonitrile on Lewis acid sites (LAS), band at 2310–2325 cm^{-1} [61].

In order to assess acid sites strength and distribution ammonia temperature-programmed desorption analysis (NH_3-TPD) was performed with a TPDRO1100 (ThermoFisher) equipped with a thermal conductivity detector (TCD). A mass of 100 mg of dried sample was loaded in a linear quartz microreactor and pretreated at 300 °C under a helium flow (20 STP $mL \cdot min^{-1}$) to remove adsorbed water. The sample was then cooled at 150 °C and saturated with a mixture of NH_3 (10 vol-%) in helium for 2 h (20 STP $mL \cdot min^{-1}$). The catalyst was purged with a helium flow at 150 °C for 1.5 h until TCD baseline stabilization to remove physiosorbed ammonia. Desorption measurement was carried out in the temperature range of 100–700 °C (10 $°C \cdot min^{-1}$, sample kept at 700 °C for 30 min) using a helium carrier (flow rate of 20 STP $mL \cdot min^{-1}$).

2.2. Experimental tests on DTO

Catalytic performance of synthesized materials was assessed by means of bench scale system able to control flowrate, temperature (up to 500 °C), and pressure (up to 30 bar). A catalytic bed (50 mg) was placed in a 4 mm (inner diameter) quartz reactor, inserted in a pressure-resistant stainless-steel jacket. The reactor assembly was heated through an electric oven. A sealed thermocouple was placed inside the reactor, in the middle of catalytic bed, to monitor and control the actual operating temperature. Prior to the catalytic test, each sample was pretreated at 380 °C (heating rate: 10 $°C \cdot min^{-1}$) for 2 h under a flow of N_2 (5 STP $mL \cdot h^{-1}$). Operating pressure was set to 2 bar and the inlet flowrate was adjusted to obtain a space time of 1 $g_{cat} \cdot h \cdot mol_C^{-1}$, by feeding a 3 vol-% DME in N_2 mixture from certified cylinder (Linde). Catalytic behavior was evaluated at four temperature values (300, 325, 350 and 375 °C) and fresh catalyst sample was used for any test. Time-on-Stream (TOS) tests up to ≈ 14 h were carried out to investigate the catalyst deactivation and the time-evolution of the products stream composition. Gas analysis consists of a gas chromatograph equipped with two columns (HP-5 and HP-PLOT/Q) to properly separate non condensable gases and light hydrocarbons, a thermal conductivity detector (TCD) and a flame ionization detector (FID).

DME conversion (ζ_{DME}), as well as yield (η_i) and selectivity (σ_i) for the generic i-th product were calculated according to the following formula:

$$\zeta_{DME} = \frac{\dot{n}_{DME,in} - \dot{n}_{DME,out}}{\dot{n}_{DME,in}} \quad (2)$$

$$\eta_i = \frac{\dot{n}_{C,i,out}}{\dot{n}_{C,in}} = \frac{N_{C,i} \cdot \dot{n}_{i,out}}{2 \cdot \dot{n}_{DME,in}} \quad (3)$$

$$\sigma_i = \frac{\dot{n}_{C,i,out}}{\dot{n}_{C,conv}} = \frac{N_{C,i} \cdot \dot{n}_{i,out}}{2 \cdot \left(\dot{n}_{DME,in} - \dot{n}_{DME,out} \right)} \quad (4)$$

Where $\dot{n}_{DME,in}$ and $\dot{n}_{DME,out}$ are inlet and outlet dimethyl ether molar flow rate, respectively. $N_{c,i}$ is the number of carbon atoms in the i-produced species, evaluating the yield and selectivity on carbon atoms balance instead of a stochiometric relationships.

If j represents the hydrocarbon class, including all the species/isomers with the same number of carbon atoms j, for a carbon-atoms number between C_2 and C_5 the olefin share OS_j has been calculated as the ratio between olefins flow rate and the whole hydrocarbon production at fixed j (i.e., paraffins and olefins).

$$OS_j = \frac{\dot{n}_{j,OLEFINS}}{\dot{n}_{j,OLEFINS} + \dot{n}_{j,PARAFFINS}} \quad (5)$$

FID calibration for the most relevant light hydrocarbons (i.e., methane, ethylene, ethane, propylene, propane, 1-butylene, n-butane, 1-pentene, and n-pentane) was performed using certified cylinders (SIAD), whilst for the other compounds, the FID response factor was estimated according to an already published procedure [62].

To measure the amount of coke deposited overspent catalysts after catalytic tests, thermogravimetric analyses were performed (SDT 650, TA Instruments). The quantity of coke was associated to the weight loss in the temperature range 150–850 °C. GC–MS (Agilent 7820A, MSD 5977E) analysis supplied qualitative information about soluble coke species formed during the TOS analyses. 10 mg of spent zeolite was firstly dissolved using HF and then soluble coke was extracted using dichloromethane as solvent [63].

3. Results and discussion

3.1. Catalysts characterization

XRD analysis results are showed in Fig. 1. Patterns of parent and passivated zeolites exhibited the typical peaks of an MFI structure (identical for Sil-1 and ZSM zeolites) and no other competitive phases were observed. Moreover, the obtained patterns demonstrate that the passivation procedure did not affect samples crystallinity as the structure was preserved with no deposition of amorphous layers.

AAS results are summarized in Table 1. The effect of passivation process was evident in the increase of the Si/Al ratio of the passivated samples, confirming that the synthesis of Silicalite-1 successfully occurred over the ZSM-5 zeolites surface. Starting from the cell composition of a ZSM-5 zeolite ($H_nAl_nSi_{96-n}O_{192}$) and knowing the Si/Al ratios of passivated (PAS_25 and PAS_50) and non-passivated samples (ZSM5_25 and ZSM5_50), it was possible to theoretically estimate the weight percentage of the synthesized Silicalite-1 layer and results are reported in Table 1 [64].

Physical properties of the catalysts, estimated through N_2 adsorption/desorption isotherms at ≈ −196 °C (77 K), are also showed in Table 1. Results obtained are aligned with data published in the open literature about ZSM-5 zeolites [65].

Specific surface area, micropore area and micropore volume values increased after the growth of Silicalite-1 over the core surface whilst the external surface significantly decreased, representing a further proof of the successful passivation process without altering the catalysts properties [60]. Whatever the Si/Al ratio of parent zeolite, the observed

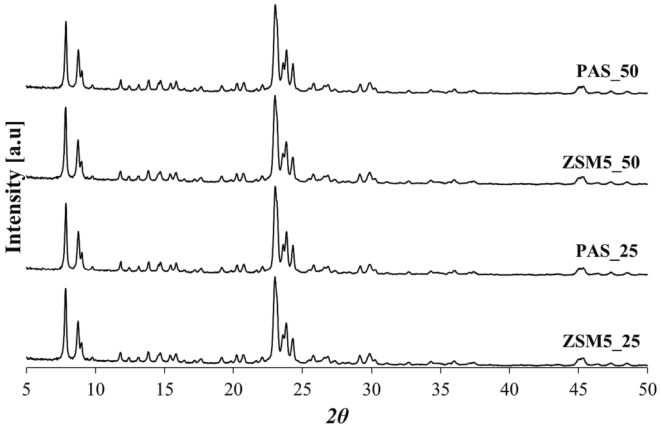

Fig. 1. XRD pattern of the investigated samples.

Table 1
Chemical composition and textural properties of zeolite catalysts.

SAMPLE	Si/Al (mol/mol)	Deposited shell (wt.-%)	S_{BET} [a] ($m^2 \cdot g^{-1}$)	S_{micro} [b] ($m^2 \cdot g^{-1}$)	S_{ext} [b] ($m^2 \cdot g^{-1}$)	V_{micro} [c] ($cm^3 \cdot g^{-1}$)
ZSM5_25	23	–	408	248	160	0.129
PAS_25	26	5.5	432	294	138	0.134
ZSM5_50	44	–	424	229	196	0.131
PAS_50	52	7.7	444	296	149	0.136

[a] Calculated by the multipoint BET method in the Rouquerol p/p0 range.
[b] Calculated by the t-plot method.
[c] Calculated by the Density Functional Theory (DFT) model.

improvement of microporous features after Sil-1 deposition confirmed that the use of a templated-ZSM-5 core promoted a rational growth of Silicalite-1 layer in continuity with the core MFI structure [60]. This ordered growth prevails over a random Silicalite-1 surface crystallization that might lead to a reduction of the pore volume as consequence of a partial pore blocking [60]. Figure S1 in the Supporting Information file presents the adsorption/desorption isotherms for the investigated catalysts.

Samples SEM micrographs are reported in Fig. 2. Investigated catalysts were characterized by small crystals of about 1 μm that aggregate forming round-shaped agglomerates with a size ranging from 5 to 20 μm. This morphology was already observed in other synthetized ZSM-5 samples published elsewhere [66]. No evident differences can be highlighted between the morphology of ZSM-5 parent zeolites and passivated catalysts because the layer of Silicalite-1 is characterized by equally small crystals, having grown on ZSM-5 crystal. EDX analysis results (Figure S2) represent a proof that passivation techniques worked successfully. Passivated catalysts always exhibited a Si/Al ratio higher than the one detected for the starting non-passivated zeolites. Moreover, the increase of Si/Al ratio found for coated samples was the highest when a voltage of 5 kV was applied (i.e., when the Si/Al ratio of samples surfaces were compared). This evidence well demonstrated the grown of a thin Silicalite-1 layer over the surface of the starting ZSM-5 zeolites.

FT-IR spectra collected after d_3-acetonitrile chemisorption are reported in Figure S3, exhibiting the typical bands of Lewis acid sites originated from aluminium at 2310–2325 cm^{-1} and of Brønsted acid sites (BAS) at 2294–2299 cm^{-1}. Deconvolution results are summarized in Table 2 and revealed that the effect of the growth of a Silicalite-1 layer on the overall acidity is appreciable only for the samples with Si/Al ratio = 25. In fact, despite the increase in the Si/Al ratio, no significant differences on the total acidity value were measured between ZSM5_50 and

Table 2
Brønsted (BAS) and Lewis (LAS) acid sites distribution of the catalysts via FT-IR measurements.

SAMPLE	BAS (μmol g_{cat}^{-1})	LAS (μmol g_{cat}^{-1})	BAS + LAS (μmol g_{cat}^{-1})	BAS/LAS ratio (–)
ZSM5_25	438	132	**570**	3.3
PAS_25	387	76	**463**	5.1
ZSM5_50	270	49	**319**	5.5
PAS_50	276	46	**322**	6.0

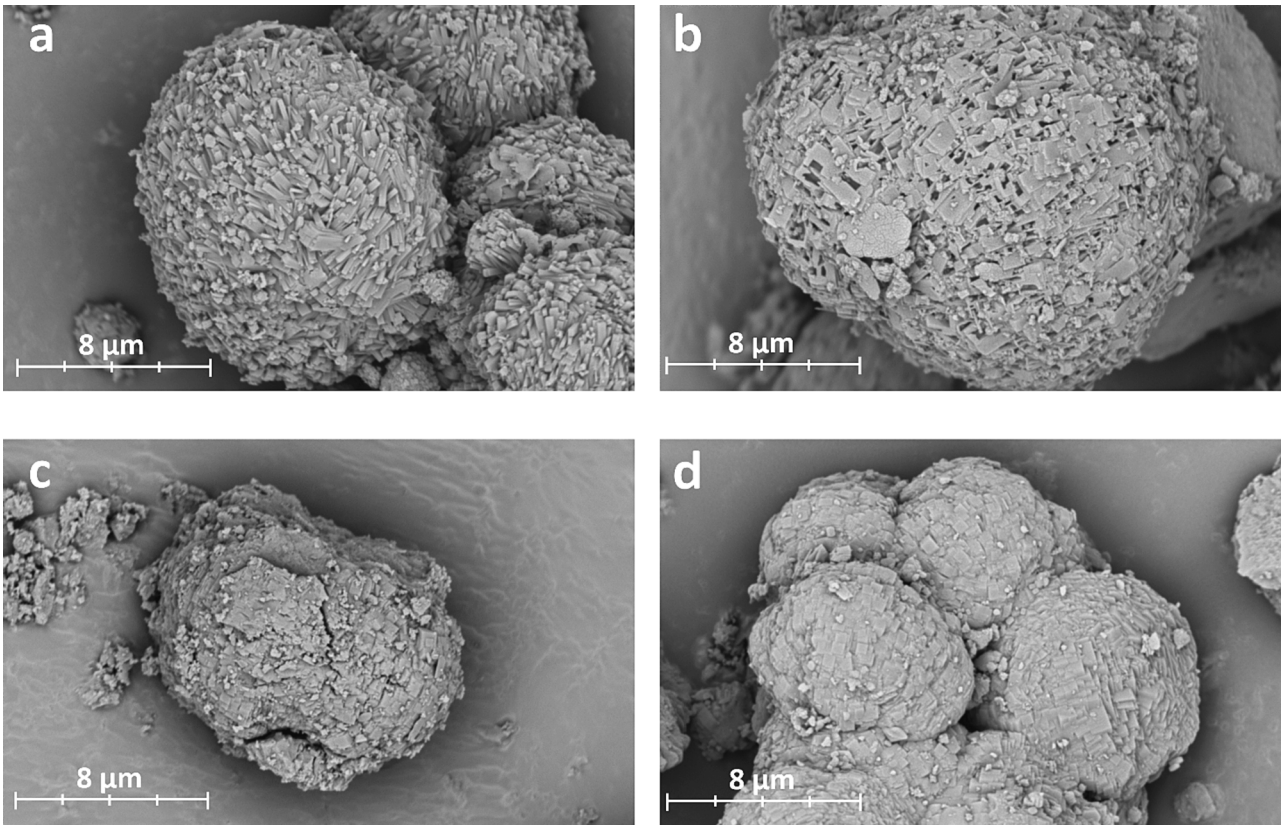

Fig. 2. SEM micrographs (obtained with a voltage of 5 kV) for ZSM5_25 (a), PAS_25 (b), ZSM5_50 (c) and PAS_50 (d).

PAS_50 samples. This evidence is in accordance with findings of open literature [67] showing that no bridging Si-(OH)-Al sites were found on the external surface of ZSM-5 and strong BAS are thus confined in the internal channels of zeolites. Moreover, the same authors proved that two types of Lewis acid sites exist on the surface of ZSM-5: LAS bonded to tetrahedrally or trigonally coordinated Al^{3+} cations and LAS due to extra framework alumina species with incompletely coordinated octahedral Al^{3+} cations. The first ones are stronger, and they are much more abundant as the Si/Al ratio of the zeolites decreases [67].

Indeed, the effect of the passivation procedure over the parent zeolite with a Si/Al ratio equal to 25 was greater for LAS which decreased by approximately 42 % than for BAS which decreased by only 11.5 %, as also demonstrated by the different increase of the BAS/LAS ratio. Sample ZSM5_50 already had a much lower number of LAS than ZSM5_25 and an even smaller number of strong LAS on the surface, as consequence. For this reason, in the case of PAS_50, no reduction of LAS was observed, induced by the Silicalite-1 deposition.

NH_3-TPD profiles of the catalysts are reported in Figure S4. Parent zeolites and passivated samples exhibited the same NH_3-TPD profiles with two main desorption peaks: the first one at lower temperatures related to weak acid sited and the second one at higher temperatures associated to strong acid sites [68]. Moreover, peaks deconvolution results are summarized in Table S1. Only a slight decrease in total acidity (5 % for PAS_25 and 7 % for PAS_50 with respect to the starting parent

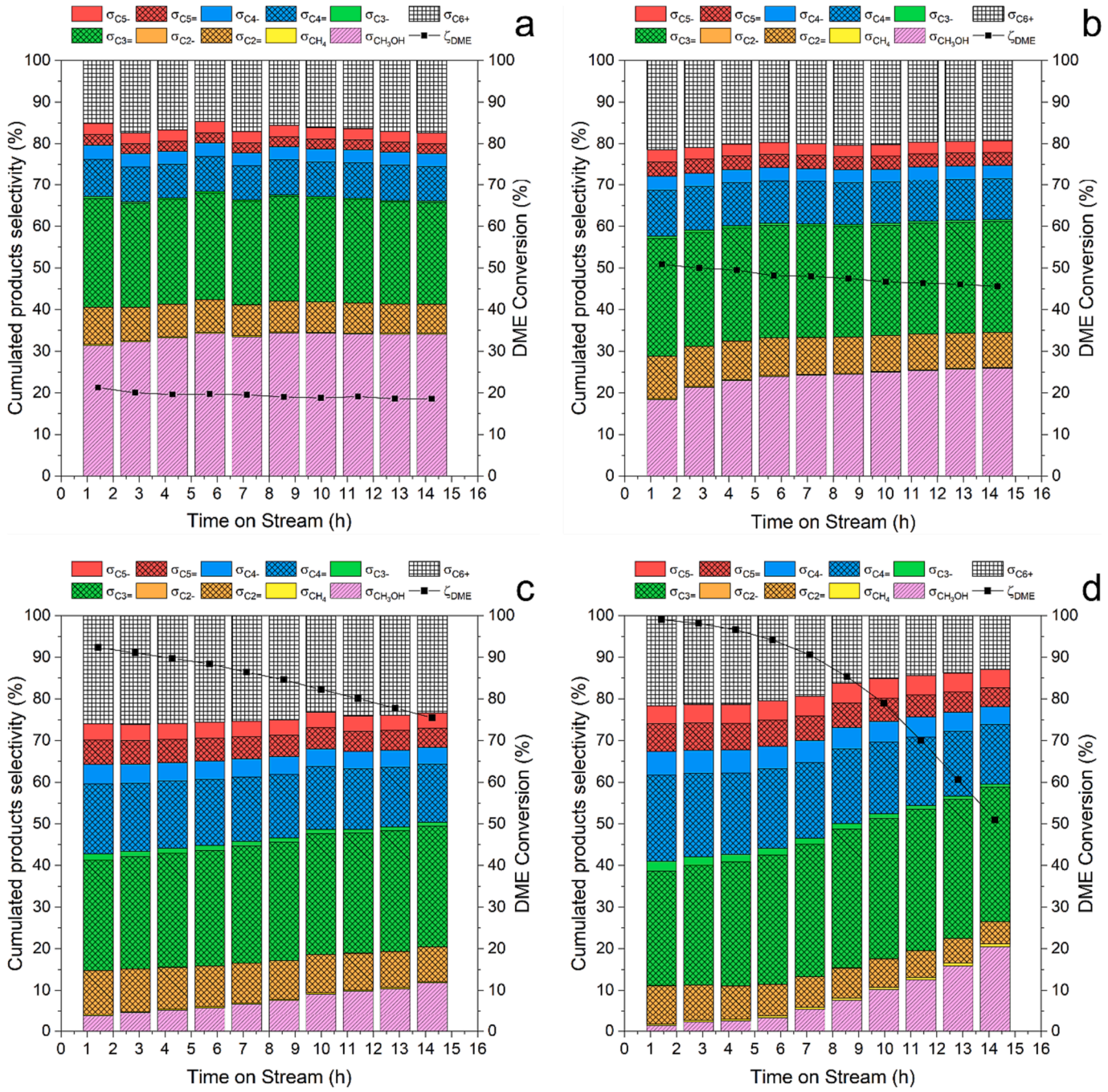

Fig. 3. Product distribution (colored bars) and DME conversion (black line) over time on stream for ZSM5_25 sample at 300 °C (a), 325 °C (b), 350 °C (c) and 375 °C (d). Olefins selectivity in the range C_2-C_5 are represented with bars having a double diagonal texture. The first pink bar from the bottom represents methanol selectivity. (For interpretation of the references to colour in this figure legend, the reader is referred to the web version of this article.)

zeolites) was detected, due to low thickness of the layer of Silicalite-1 (see Table 1). Moreover, results demonstrated that passivation procedure did not affect the ratio between strong and weak acid sites which was almost unchanged after the coating with Silicalite-1.

3.2. DTO experimental tests

3.2.1. Time-on-stream analysis and product distribution

The following section will present the results of the time-on-stream tests performed on the parent (ZSM5_25 and ZSM5_50) and passivated zeolites (PAS_25 and PAS_50) in the DME-to-Olefins reaction. Fig. 3 shows both the DME conversion profile and the distribution of obtained products (through their selectivity) for the non-passivated ZSM5_25 at the different reaction temperatures. Supporting Information file reports the same charts for all the investigated samples. The lumped group C_{6+} accounts for all the hydrocarbon species having a carbon atoms number equal or greater than 6 including paraffins, olefins and aromatics (e.g., toluene, xylenes and other polymethyl benzenes).

As expected, the initial conversion (TOS = 1.5 h) rises when increasing the reaction temperature is increased due to a kinetic effect. Whatever the temperature, the DME conversion decreases over time, even though the effect is more pronounced at 350 °C and 375 °C (50 % drop after 14 h). Such fast deactivation implies that, after 10 h, DME conversion at 350 °C overcomes the value at 375 °C. In addition, resulting from acid-catalyzed DME hydration reaction, methanol was detected in considerable amount within the produced gas [65,69,70]. In presence of the water produced from DTO reaction pathways, the DME hydration to methanol is a relevant reaction when the DME conversion is low over time (i.e., at lor temperature, Fig. 3-a and Fig. 3-b). The analysis of gas products at the earliest stage of TOS (about 1.5 h of reaction) reported a CH_3OH selectivity decrease when increasing the reaction temperature: namely ≈ 31 %, 18 %, 4 % and 1 % at 300, 325, 350 and 375 °C, respectively. This suggests that methanol it is easily formed at low temperatures via DME conversion, but the alcohol is also involved in the reaction pathway leading to hydrocarbons production that start to be relevant when increasing the temperature. It is worth noting that methanol production increases overt time during TOS test and this effect is more pronounced at temperature above 350 °C. Since this effect is observed together with a decrease of the DME conversion, a coherent explanation of this behavior is related to the formation of coke species clogging the zeolite pores, partially hindering the reaction pathways of olefins formation that take place via “Hydrocarbon pool” mechanism that involves polymethyl-benzenes as intermediate [71]. The reduced amount of available acid sites seems to have stronger impact on the reaction pathways leading to hydrocarbon species formation than to methanol production.

Moreover, hydrocarbon formation over acid zeolites have been extensively investigated when methanol is used as reactant in the MTO process. A dual cycle hydrocarbon pool mechanism has been proposed for the formation of olefins, paraffins and aromatics [72,73]. Olefins like propene, butenes and heavier ones should be produced via consecutive olefin methylation and cracking, representing the alkenes cycle [73]. H-transfer and cyclization lead to the conversion of olefins into paraffins and aromatic and represent the link between olefin-based cycle and aromatic-based cycle [72]. Aromatic methylation and dealkylation are responsible for the formation of olefins (mainly ethylene) and polymethyl benzenes.

When DME is used as primary reactant, according to the calculated selectivity (Fig. 3), propylene is the most abundant hydrocarbon at every tested temperature and for each investigated catalyst. This result is in good agreement with other literature findings, showing that propylene is the olefin presenting the highest selectivity when DTO tests is carried out using HZSM-5 as catalyst, especially at low space velocity [32,45,46]. This evidence is opposite to the MTO processes using SAPO-34 (industrial benchmark) as catalyst where ethylene-to-propylene ratio (*E/P*) above 1 is always found, because the narrow pores of this structure promote a different shape selectivity [33,37]. In addition, catalyst deactivation led to a monotonic decrease in ethylene and butenes selectivity, whilst propylene selectivity rose presenting a maximum after 11 h of TOS at 375 °C, followed by a slight decrease. Such trends suggest that deactivation has a stronger impact on steps like C_2H_4 formation from aromatic-based cycle and propene methylation to butenes.

In the Supporting Information file (Figure S5-S7) the catalytic results for all the other samples are reported at any investigated temperature.

To assess the effect of acidity and surface passivation, Fig. 4 reports the data of the tests performed at 375 °C. What stands out from the comparison (Fig. 4-a and Fig. 4-c) is that a lower overall acidity of the catalysts implies a lower initial conversion and a superior stability over time, as well as higher methanol selectivity at the beginning of TOS. As presented in the previous paragraph, when the DME conversion drops over time the methanol concentration in the product stream increases, and this could be attributed to the catalyst deactivation that negatively affect both Methanol- and DME-To-Olefins reaction pathways. This effect is more evident for the ZSM5_25 samples (Fig. 4-a and Fig. 4-b) where the effect of the overall acidity on the deactivation is also evident: the higher is the acidity the faster the deactivation and the greater the methanol presence as consequence. An additional amount of acid sites for ZSM5_25 and PAS_25 seem to preferentially drive the reaction mechanism towards hydrocarbon formation. Passivation procedure with Silicalite-1 applied to MFI structure with Si/Al atomic ratio equal to 25 improve the catalyst stability; reduced deactivation at 375 °C is more evident for PAS_25 with respect to the ‘parent’ sample ZSM5_25 (Fig. 4-a and Fig. 4-b). Such a behavior could be related to the mechanism of coke formation and the reduced surface acidity. Catalytic assessment of pure Silicalite-1 was performed in the temperature range 300–360 °C, using methanol as fed reactant. Even though the space velocity (≈ 9 g_{cat} h mol_C^{-1}) was significantly higher than the one applied in DTO campaign, very low conversion (up to 7 %) was obtained. Furthermore, the only detected product was DME, with no evidence of hydrocarbons formation in presence of Silicalite-1.

It has been reported that when MFI structures like are used at temperature above 350 °C, the formed coke is mainly graphitic/non soluble and its formation occurs on the external surface of the crystallites, then clogging the pores access [72]. If coke was partly generated by precursors formed onto the acid sites outside the pores, superficial passivation of external acidity would represent a strategy to counteract deactivation process [72]. Furthermore, the other tested samples (especially PAS_25) also present an increase in methanol selectivity as the DME conversion decreases over time, due to the catalyst deactivation.

Propylene (green textured bar) is the most abundant hydrocarbon for all the investigated samples. According to equation (3), at 375 °C a C_3H_6 yield of 27.2 %, 26.4 %, 32.0 % and 34.0 % resulted for ZSM5_25, PAS_25, ZSM5_50 and PAS_50, respectively. Besides yield, specific propylene productivity was calculated as the outlet C_3H_6 flow rate divided by catalyst load. At a reaction temperature of 375 °C, values equal to ≈ 91, 88, 107 and 113 $mol_{propylene} \cdot kg_{cat}^{-1} \cdot h^{-1}$ were obtained for ZSM5_25, PAS_25, ZSM5_50 and PAS_50, respectively. Both propylene yield and specific productivity were evaluated through the results from the first GC run (i.e., as close as possible to the performance of a fresh catalyst). Due to catalyst deactivation, these productivity indicators could change during the time-on-stream analysis. Samples having a major Si/Al ratio presented slightly higher propylene productivity, partially related to a greater selectivity. Clearly, C_3H_6 productivity decreases at lower reaction temperatures, mainly due to the reduced DME conversion. Besides productivity, integral propylene production was calculated by integrating the C_3H_6 flow rate over the time-on-stream interval. A specific production of ≈ 53, 55, 64 and 67 g of propylene per gram of catalyst over the 14 h of TOS resulted for ZSM5_25, PAS_25, ZSM5_50 and PAS_50, respectively. It clearly appears that the lower is the catalyst acidity, the higher is the C_3 olefin productivity, also as a consequence of the reduced deactivation. Table 3 summarizes the calculated values.

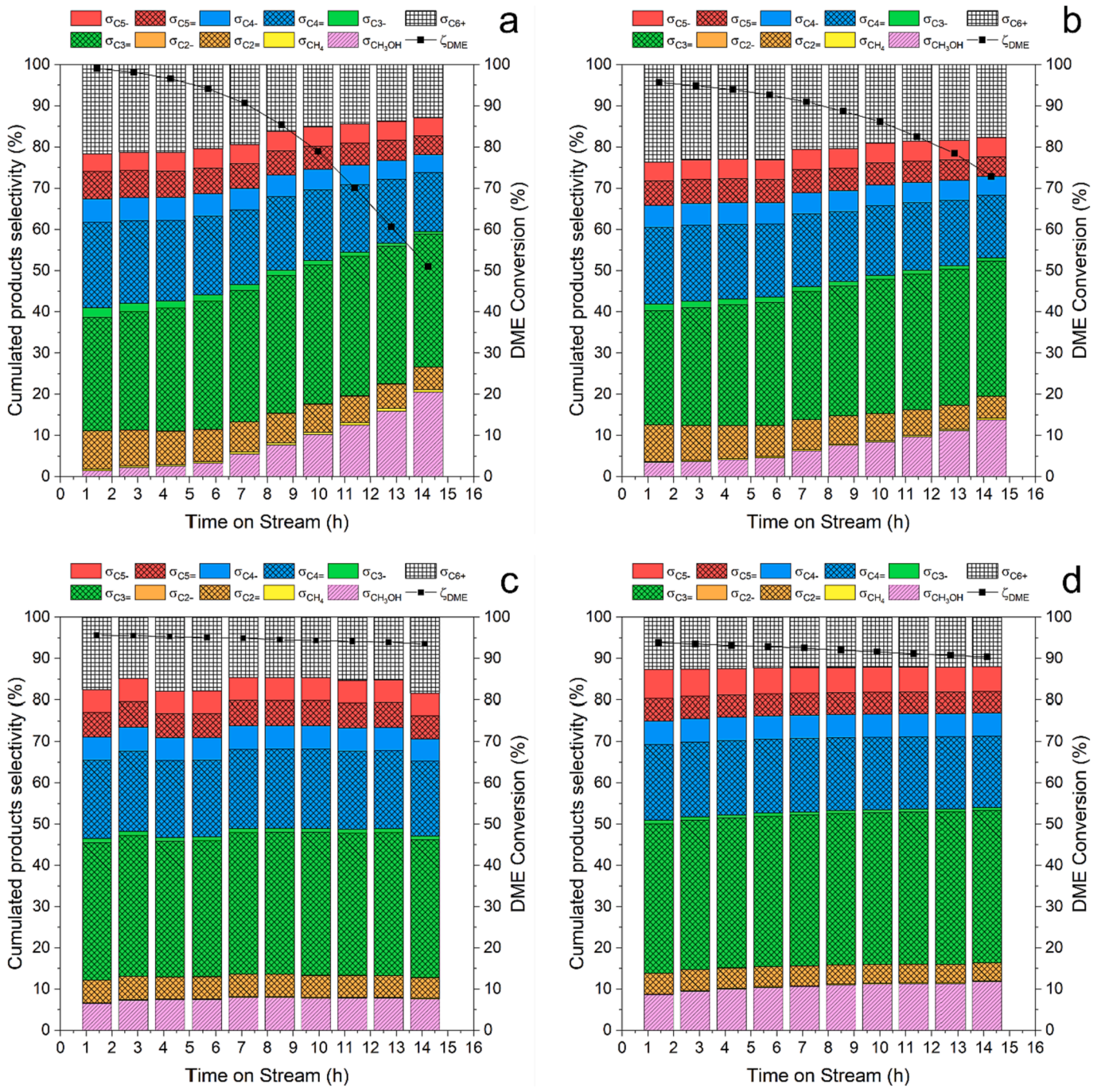

Fig. 4. Product distribution (colored bars) and DME conversion (black line) over time on stream at 375 °C for ZSM5_25 (a), PAS_25 (b), ZSM5_50 (c) and PAS_50 (d). Olefins selectivity in the range C_2-C_5 are represented with bars having a double diagonal texture. The first pink bar from the bottom represents methanol selectivity. (For interpretation of the references to colour in this figure legend, the reader is referred to the web version of this article.)

Table 3
Propylene productivity indicators evaluated at 375 °C. C_3H_6 yield and specific productivity were evaluated considering the first GC run during TOS. Integral production refers to the entire test duration.

	C_3H_6 yield	*C_3H_6 specific productivity ($mol_{propylene} kg_{cat}^{-1} h^{-1}$)*	*C_3H_6 integral production ($g_{propylene}$ g_{cat}^{-1})*
ZSM5_25	27.2 %	91	53
PAS_25	26.4 %	88	55
ZSM5_50	32.0 %	107	64
PAS_50	34.0 %	113	67

Table 4
Average light olefins selectivity ($C_{2=}$-$C_{4=}$) during TOS for each investigated catalyst at different reaction temperatures (with a space velocity of 1 g_{cat} h mol_C^{-1}).

	Light olefins selectivity			
	300 °C	**325 °C**	**350 °C**	**375 °C**
ZSM5_25	43.0 %	47.6 %	53.7 %	57.7 %
PAS_25	41.0 %	47.4 %	52.3 %	55.8 %
ZSM5_50	39.0 %	45.6 %	52.0 %	58.6 %
PAS_50	38.2 %	43.0 %	53.5 %	59.6 %

Table 4 summarizes the average value of cumulated selectivity of light olefins in the range C_2-C_4 (i.e., ethylene, propylene and butenes) for each catalyst in the temperature range 300–375 °C. and a general trend could be observed: light olefins selectivity ($\sigma_{C2=}$ - $\sigma_{C4=}$) increases with temperature for all the investigated catalysts, alongside the decrease of methanol selectivity at higher temperatures.

At low temperature values, when deactivation is almost absent and the role of acidity is clearer, the selectivity of light olefins is proportional to the overall concentration of acid sites (see also Table 2). This trend is less clear and defined at higher temperatures.

A reduction of ethylene, butenes and heavier hydrocarbons (C_{6+}) was observed besides the increase of methanol selectivity over the time when the impact of deactivation leads to an evident conversion drop (e.g., ZSM5_25 and PAS_25 at 375 °C). Such a product rearrangement could be partly explained by a stronger impact of deactivation on the aromatic-based cycle within the hydrocarbon pool mechanism, responsible for the formation of ethylene and part of C_{6+} compounds. On the other hand, butenes are mainly formed both via olefin methylation and heavier olefins cracking. Deactivation could slow down the rate of one of these steps (e.g., propylene methylation), which would be also in agreement with the increasing C_3H_6 content during TOS investigation.

The olefinic share (OS_j) for hydrocarbon classes between C_2 and C_5 has been calculated for each time-on-stream test as the ratio between olefins amount and the whole hydrocarbon production at the same C atoms number, according to equation (5). For instance, for C_3 class this parameter is obtained as the ratio between propene flow rate and propene plus propane flow rate. In Fig. 5 olefinic share at 375 °C for the investigated samples is shown.

It is worth highlighting that the olefinic share decreases as the carbon atoms number increases. This trend results from all the 16 time-on-stream investigations (four different catalysts, each one tested at four different temperatures). Olefinic share for C_2 is always close to 100 %

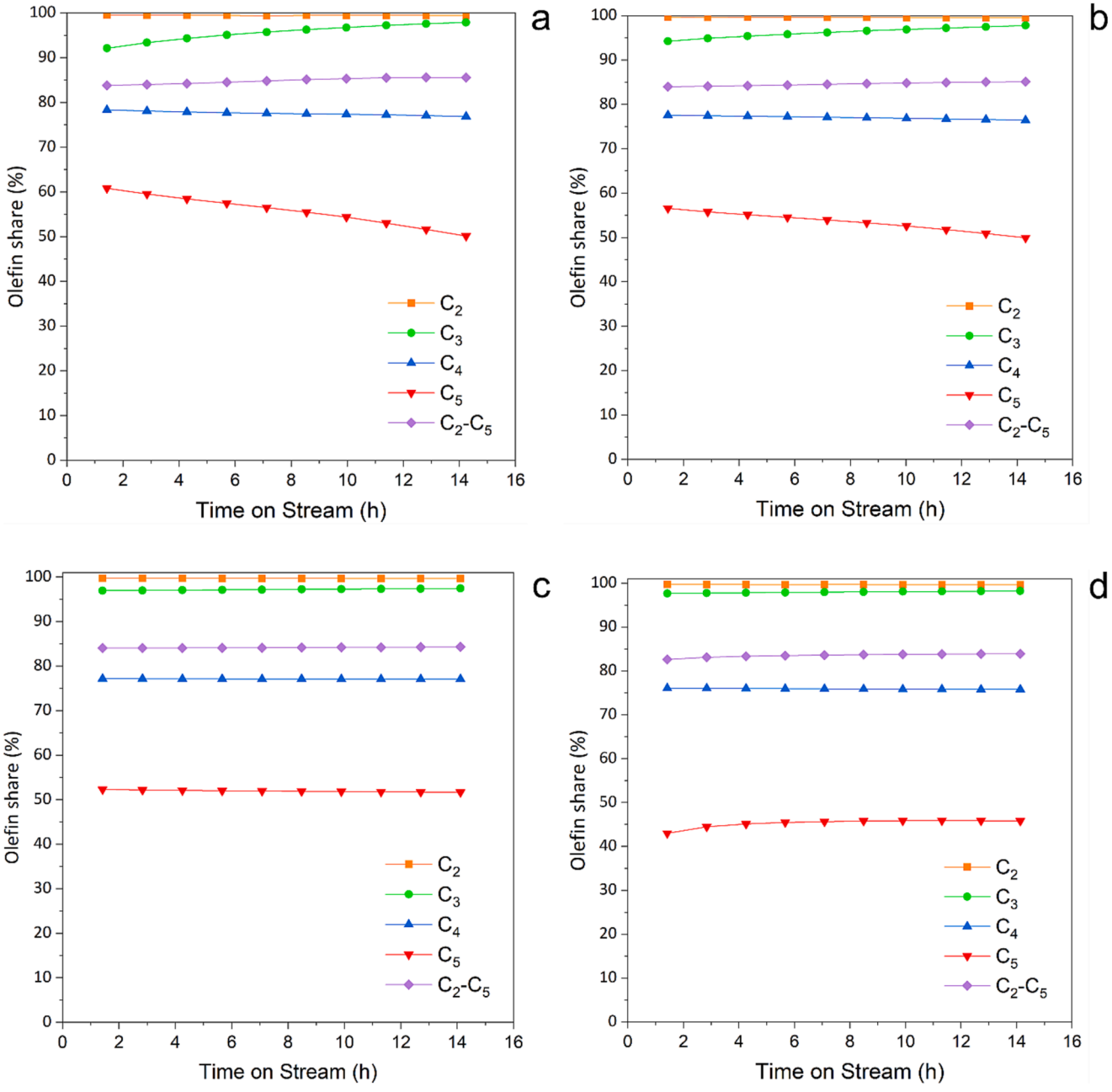

Fig. 5. Olefinic percentage for hydrocarbon classes between C_2 and C_5 at 375 °C for ZSM5_25 (a), PAS_25 (b), ZSM5_50 (c) and PAS_50 (d).

since almost no ethane was detected. The amount of paraffins is superior when the number of carbons is higher. According to the dual-cycle hydrocarbon pool mechanism, paraffins are mainly formed from olefins via hydrogen transfer reactions [72]. Since this step involves two olefins, lighter paraffins like C_2H_6 and C_3H_8 are not easily formed, while the production of alkanes from C_4 is more abundant. Thus, these results corroborate the products formation via the hydrocarbon pool mechanism [72,73].

TOS tests with faster deactivation (i.e., ZSM5_25 and ZSM5_25 at 375 °C) present a progressive increase of C_3 olefin share resulting from an increase of propylene combined with the reduction of propane production. On the other hand, olefins content for C_5 class decreases when noticeable deactivation occurs. This drop could be partly related to the aforementioned reduction in butenes content during the TOS, because pentenes can be formed (among the other pathways) via butenes methylation; however, another possible interpretation may be the impact of deactivation on heavier olefins cracking into butenes and pentenes.

The obtained experimental results showed a high amount of light olefins within the product gas, especially at higher temperature when methanol content decreases. Light olefins are more abundant than heavy compounds (C_{6+}) for each TOS experiment, indicating that alkene-cycle seems to be the preferential reaction pathway in the hydrocarbon pool mechanism when an MFI-type zeolite is used for DTO. This is also confirmed by the ethylene-to-propylene ratio (*E/P*) lower than 1, since ethylene should be formed only through the aromatic-cycle [72,73].

Light olefins selectivity grew by increasing the temperature, but higher temperatures boosted the deactivation phenomena, causing a sharp decrease of the DME conversion, especially for the samples with high acidity. Furthermore, the higher methanol content detected at low temperature implies that the DME hydration to methanol is always present but the alcohol (as well as DME) conversion to hydrocarbons is slowed down as effect of catalyst deactivation at least for the relatively low residence time used in this work.

3.2.2. Coke analysis

Thermogravimetric results of spent catalysts are summarized in Fig. 6 Percentage weight loss in the temperature range 150–850 °C has been calculated for all the investigated reaction temperatures. For what concerns ZSM5_25 and PAS_25 the prevailing trend is the increase of the weight loss (i.e., the formed coke) with the increasing of reaction temperature. Comparing spent ZSM5_25 and PAS_25 samples, the quantity of coke deposited was nearly equal at any reaction temperature below 375 °C.

However, a great difference was found when catalysts were tested at 375 °C; passivated sample (PAS_25) allowed to produce about 20 % less of coke compounds than the parent zeolite. The positive effect obtained using PAS_25 at high reaction temperature was not found for PAS_50 that produced a quantity of coke always higher than the parent zeolite (ZSM5_50). This result agrees with the hypothesis already displayed according to which the growth of Silicalite-1 over a parent zeolite with high Si/Al ratio does not modify acidity surface properties and, thus, it does not improve the catalytic performances in terms of coke formation.

Coke production can be also related to the whole amount of DME converted during the time-on-stream investigation ($mg_{coke} \cdot g_{DME,converted}^{-1}$). Total converted dimethyl ether is calculated through the numerical integration of DME conversion profile over the time and results are presented in Table 5.

The mass of formed coke referred to the converted DME decreases at temperature above 300 °C for all the investigated samples. With a more pronounced drop for samples having the zeolite core with Si/Al = 50 (MFI-50 and PAS-50). ZSM5_25 and PAS_25 showed a faster deactivation especially at 375 °C, that could be related to a great coke production which is not compensated by the higher amount of converted DME. As a general trend, catalysts with Si/Al = 50 (i.e., with a lower concentration of acid sites) present a reduced specific coke production if compared with samples having Si/Al = 25.

Fig. 7 reports DTA analysis of spent ZSM5_25 catalyst. The endothermic peak at around 100 °C refers to the evaporation of water trapped in the sample after the reaction. The combustion of coke compounds, instead, is identified by exothermic peaks and the peak temperature can give information about the coke species. At relative low reaction temperatures (300 °C – 325 °C) two exothermic peaks were identified: one at about 270 °C and another at high temperatures (≈ 540 °C). With the increasing of reaction temperature, the exothermic peak observed at relative low temperatures disappeared and moved towards higher temperatures (≈ 370 °C) whilst the peak at 540 °C remained becoming prominent and distinct. The same trend was observed for the thermogravimetric analyses of sample PAS_25, but less clearly for those of ZSM5_50 and PAS_50 spent catalysts (Figure S8), and it could be explained by the fact that, at high reaction temperatures, a ZSM5 type catalyst formed coke is composed of aromatics species bigger than those formed at low temperature [72].

Table 5
Specific coke production referred to the overall amount of converted dimethyl ether.

	Formed coke ($mg_{coke} \cdot g_{DME,\ converted}^{-1}$)			
	300 °C	**325 °C**	**350 °C**	**375 °C**
ZSM5_25	0.84	0.29	0.23	0.35
PAS_25	0.85	0.31	0.23	0.26
ZSM5_50	0.44	0.15	0.12	0.11
PAS_50	0.69	0.26	0.17	0.16

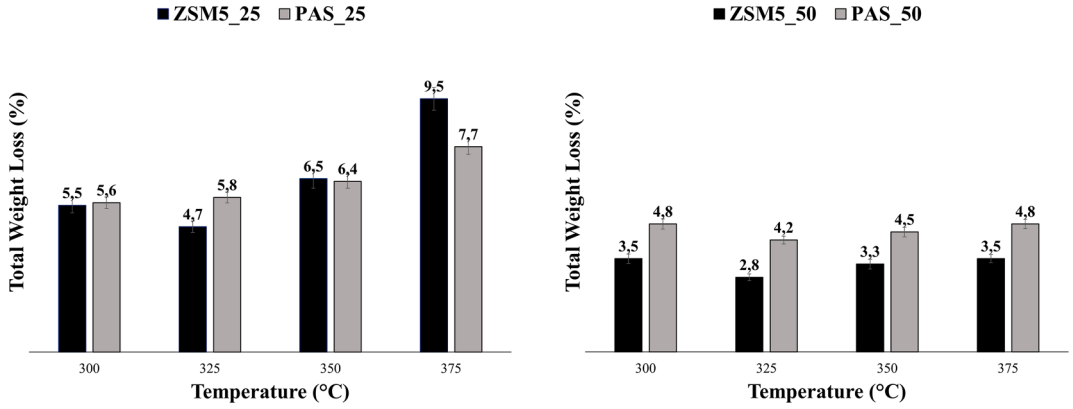

Fig. 6. Coke amount for each investigated sample in the whole reaction temperature range; on the left core Si/Al ratio equal to 25, on the right core Si/Al ratio equal to 50.

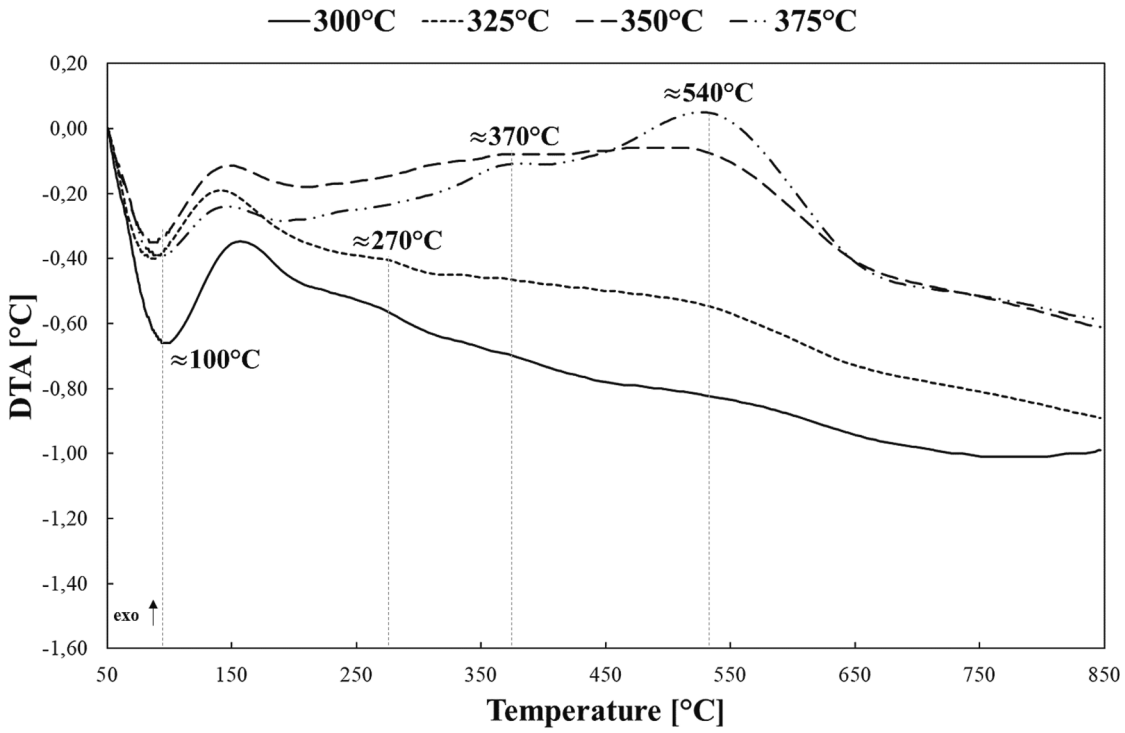

Fig. 7. Differential thermal analysis results of ZSM5_25 sample.

This evidence agrees with results obtained from GC–MS analysis of soluble extracted species (Figure S9). Although the deactivation of the catalysts was much more evident at high reaction temperatures after 16 h of time-on-stream, non-soluble aromatics were formed. Conversely, the abundance of compounds detected by GC–MS decreased with increasing reaction temperatures, demonstrating that catalyst deactivation resulted from the formation of big coke compounds not soluble in CH_2Cl_2 and partly formed on the surface of ZSM-5 samples.

Acidity of a regenerated sample was additionally investigated. Spent PAS_25 (tested at 350 °C) was regenerated through TGA under an air flow of 100 STP mL•min^{-1}. The sample was heated up to a temperature of 650 °C (until no weight change was further detected) and kept at this temperature for one hour. Acid sites concentration of the regenerated sample was assessed again via FT-IR analysis involving d_3-acetonitrile as probe. The comparison between the acidity of regenerated catalyst and its corresponding fresh sample is reported in Table 6. A slight decrease in Brønsted acid sites concentration was observed after the zeolite regeneration. This could be due to the high temperature reached during catalyst recycling (via coke combustion) which could lead to silanol dehydroxylation, generally detected at temperatures above 550 °C. The lack of the band at 2275 cm^{-1} (usually associated to external silanols linked to d_3-acetonitrile) for the regenerated sample (Figure S10) is a further prove that silanols dehydroxylation occurred.

4. Conclusion

In order to assess the role of acidity and surface- passivation, this work investigated the DTO process over zeolites, with a focus on light olefins in the range C_2-C_4. Four catalysts were tested: MFI-type zeolites with Si/Al ratio equal to 25 and 50, and the corresponding core–shell samples where the ZSM-5 core (in as made form) was passivated through a Silicalite-1 layer deposition. Showing an increase in the Si/Al ratio for passivated samples, the atomic absorption measurements confirmed the growth of the Silicalite-1 layer on the starting parent zeolites and acidity characterizations of catalysts demonstrated a greater effect of the surface passivation technique on the zeolite with a Si/Al ratio equal to 25.

Each sample was tested in the temperature range 300–375 °C and kept under reaction condition for 16 h of time-on-stream. Light olefins (i.e., ethylene, propylene and butenes) overall selectivity was up to 60 %, but a considerable amount of methanol was still unconverted especially at lower temperatures. For each investigated sample propylene was the most abundant product, reaching a selectivity of about 35 %, suggesting that the alkene cycle of hydrocarbon pool mechanism is the predominant reaction pathway. The relatively low amount of paraffins detected seems to corroborate this conclusion. DME conversion obtained at a space time of 1 g_{cat}·h·mol$_C^{-1}$ with MFI-type zeolites is higher than the values reported for other zeolite catalysts like SAPO-34.

Passivation of HZSM-5 core having Si/Al = 25 improved the catalyst stability, reducing its deactivation especially at high reaction temperature, suggesting that at least part of coke formation should occur on the crystal surface outside the pores. Besides this aspect, also the lower acidity induced by the passivation may play a role in obtaining a slower deactivation over time.

Especially at high temperature, samples with Si/Al ratio equal to 50 showed higher stability but, on the other hand, higher methanol selectivity and slightly lower initial activity.

Future investigation should focus on testing catalysts at different space velocity to evaluate the impact of residence time on product

Table 6
Brønsted (BAS) and Lewis (LAS) acid sites distribution of the PAS_25 fresh and regenerated sample via FT-IR measurements.

SAMPLE	BAS (μmol g_{cat}^{-1})	LAS (μmol g_{cat}^{-1})	BAS + LAS (μmol g_{cat}^{-1})
Fresh	387	76	**463**
Regenerated	326	81	**411**

distribution/selectivity.

CRediT authorship contribution statement

Emanuele Giglio: Data curation, Formal analysis, Investigation, Methodology, Software, Visualization, Writing – original draft. **Giorgia Ferrarelli:** Data curation, Formal analysis, Investigation, Methodology, Visualization, Writing – original draft. **Fabio Salomone:** Data curation, Formal analysis, Investigation, Software, Writing – original draft. **Elena Corrao:** Data curation, Investigation, Methodology, Software. **Massimo Migliori:** Conceptualization, Formal analysis, Methodology, Supervision, Writing – review & editing. **Samir Bensaid:** Conceptualization, Funding acquisition, Project administration, Resources. **Raffaele Pirone:** Conceptualization, Resources, Supervision. **Girolamo Giordano:** Conceptualization, Funding acquisition, Resources, Supervision.

Declaration of competing interest

The authors declare that they have no known competing financial interests or personal relationships that could have appeared to influence the work reported in this paper.

Data availability

Data will be made available on request.

Acknowledgements

The authors gratefully acknowledge the Italian Ministry of University and Research (MUR), program PNR 2015-2020 (D.D. 1735 10.072017) “Industrial research in the 12 areas of specialization”, specialization area “Energy”, Project “WWGF - Gasification of Wet Organic Waste with Supercritical Water for the Production of Biomethane and LNG”, grant number ARS01_00868, for work co-founding.

F.S. also acknowledges the Italian Ministry of University and Research (MUR), program FSE REACT-EU PON Ricerca e Innovazione 2014-2020 (D.M. 1062/2021). This manuscript reflects only the authors’ views and opinions, neither the European Union nor the European Commission can be considered responsible for them.

Appendix A. Supplementary data

Supplementary data to this article can be found online at https://doi.org/10.1016/j.fuel.2023.130559.

References

[1] IEA. Key World Energy Statistics; 2021.
[2] BP. Statistical Review of World Energy; 2022.
[3] Giglio E, Pirone R, Bensaid S. Dynamic modelling of methanation reactors during start-up and regulation in intermittent power-to-gas applications. Renew Energy 2021;170:1040–51. https://doi.org/10.1016/j.renene.2021.01.153.
[4] Giglio E, Vitale G, Lanzini A, Santarelli M. Integration between biomass gasification and high-temperature electrolysis for synthetic methane production. Biomass Bioenergy 2021;148:106017. https://doi.org/10.1016/j.biombioe.2021.106017.
[5] Morosanu EA, Salomone F, Pirone R, Bensaid S. Insights on a Methanation Catalyst Aging Process: Aging Characterization and Kinetic Study. Catalysts 2020;10:283. https://doi.org/10.3390/catal10030283.
[6] Mazza A, Salomone F, Arrigo F, Bensaid S, Bompard E, Chicco G. Impact of Power-to-Gas on distribution systems with large renewable energy penetration. Energy Conversion and Management: X 2020;7:100053. https://doi.org/10.1016/j.ecmx.2020.100053.
[7] Salomone F, Giglio E, Ferrero D, Santarelli M, Pirone R, Bensaid S. Techno-economic modelling of a Power-to-Gas system based on SOEC electrolysis and CO2 methanation in a RES-based electric grid. Chem Eng J 2019;377:120233. https://doi.org/10.1016/j.cej.2018.10.170.
[8] Marchese M, Giglio E, Santarelli M, Lanzini A. Energy performance of Power-to-Liquid applications integrating biogas upgrading, reverse water gas shift, solid oxide electrolysis and Fischer-Tropsch technologies. Energy Conversion and Management: X 2020;6:100041. https://doi.org/10.1016/j.ecmx.2020.100041.
[9] Marchese M, Heikkinen N, Giglio E, Lanzini A, Lehtonen J, Reinikainen M. Kinetic Study Based on the Carbide Mechanism of a Co-Pt/γ-Al_2O_3 Fischer-Tropsch Catalyst Tested in a Laboratory-Scale Tubular Reactor. Catalysts 2019;9:717. https://doi.org/10.3390/catal9090717.
[10] Gao X, Atchimarungsri T, Ma Q, Zhao T-S, Tsubaki N. Realizing efficient carbon dioxide hydrogenation to liquid hydrocarbons by tandem catalysis design. EnergyChem 2020;2:100038. https://doi.org/10.1016/j.enchem.2020.100038.
[11] Yao B, Xiao T, Makgae OA, Jie X, Gonzalez-Cortes S, Guan S, et al. Transforming carbon dioxide into jet fuel using an organic combustion-synthesized Fe-Mn-K catalyst. Nat Commun 2020;11:6395. https://doi.org/10.1038/s41467-020-20214-z.
[12] Azhari NJ, Nurdini N, Mardiana S, Ilmi T, Fajar ATN, Makertihartha IGBN, et al. Zeolite-based catalyst for direct conversion of CO_2 to C_{2+} hydrocarbon: A review. J CO2 Util 2022;59:101969. https://doi.org/10.1016/j.jcou.2022.101969.
[13] Cordero-Lanzac T, Ramirez A, Cruz-Fernandez M, Zander H-J, Joensen F, Woolass S, et al. A CO_2 valorization plant to produce light hydrocarbons: Kinetic model, process design and life cycle assessment. J CO2 Util 2023;67:102337. https://doi.org/10.1016/j.jcou.2022.102337.
[14] Ticali P, Salusso D, Airi A, Morandi S, Borfecchia E, Ramirez A, et al. From Lab to Technical CO_2 Hydrogenation Catalysts: Understanding PdZn Decomposition. ACS Appl Mater Interfaces 2023;15:5218–28. https://doi.org/10.1021/acsami.2c19357.
[15] Corrao E, Salomone F, Giglio E, Castellino M, Ronchetti SM, Armandi M, et al. CO_2 conversion into hydrocarbons via modified Fischer-Tropsch synthesis by using bulk iron catalysts combined with zeolites. Chem Eng Res Des 2023;197:449–65. https://doi.org/10.1016/j.cherd.2023.07.052.
[16] Bozzano G, Manenti F. Efficient methanol synthesis: Perspectives, technologies and optimization strategies. Prog Energy Combust Sci 2016;56:71–105. https://doi.org/10.1016/j.pecs.2016.06.001.
[17] Guzmán H, Salomone F, Bensaid S, Castellino M, Russo N, Hernández S. CO_2 Conversion to Alcohols over Cu/ZnO Catalysts: Prospective Synergies between Electrocatalytic and Thermocatalytic Routes. ACS Appl Mater Interfaces 2022;14:517–30. https://doi.org/10.1021/acsami.1c15871.
[18] Guzmán H, Salomone F, Batuecas E, Tommasi T, Russo N, Bensaid S, et al. How to make sustainable CO_2 conversion to Methanol: Thermocatalytic versus electrocatalytic technology. Chem Eng J 2021:417. https://doi.org/10.1016/j.cej.2020.127973.
[19] Parigi D, Giglio E, Soto A, Santarelli M. Power-to-fuels through carbon dioxide Re-Utilization and high-temperature electrolysis: A technical and economical comparison between synthetic methanol and methane. J Clean Prod 2019;226:679–91. https://doi.org/10.1016/j.jclepro.2019.04.087.
[20] Schiaroli N, Negahdar L, Lützen M, Hoang Ho P, Allen LJ, Natoli A, et al. Efficient low-loaded ternary Pd-In_2O_3-Al_2O_3 catalysts for methanol production. J Catal 2023;424:140–51. https://doi.org/10.1016/j.jcat.2023.05.012.
[21] Ding R, Fu G, Wang S, Yang Y, Lang Q, Zhao H, et al. The Activity of Ultrafine Cu Clusters Encapsulated in Nano-Zeolite for Selective Hydrogenation of CO_2 to Methanol. Catalysts 2022;12:1296. https://doi.org/10.3390/catal12111296.
[22] Leonzio G. State of art and perspectives about the production of methanol, dimethyl ether and syngas by carbon dioxide hydrogenation. J CO2 Util 2018;27:326–54. https://doi.org/10.1016/j.jcou.2018.08.005.
[23] Ateka A, Rodriguez-Vega P, Ereña J, Aguayo AT, Bilbao J. A review on the valorization of CO_2. Focusing on the thermodynamics and catalyst design studies of the direct synthesis of dimethyl ether. Fuel Process Technol 2022;233:107310. https://doi.org/10.1016/j.fuproc.2022.107310.
[24] Salomone F, Bonura G, Frusteri F, Castellino M, Fontana M, Chiodoni AM, et al. Physico-Chemical Modifications Affecting the Activity and Stability of Cu-Based Hybrid Catalysts during the Direct Hydrogenation of Carbon Dioxide into Dimethyl-Ether. Materials 2022;15:7774. https://doi.org/10.3390/ma15217774.
[25] Hirota Y, Murata K, Miyamoto M, Egashira Y, Nishiyama N. Light olefins synthesis from methanol and dimethylether over SAPO-34 nanocrystals. Catal Letters 2010;140:22–6. https://doi.org/10.1007/s10562-010-0421-1.
[26] Xie J, Firth DS, Cordero-Lanzac T, Airi A, Negri C, Øien-Ødegaard S, et al. MAPO-18 Catalysts for the Methanol to Olefins Process: Influence of Catalyst Acidity in a High-Pressure Syngas (CO and H_2) Environment. ACS Catal 2022;12:1520–31. https://doi.org/10.1021/acscatal.1c04694.
[27] Wu P, Fan D, Liu L, Yang M, Tian P, Liu Z. Synthesis of SAPO-34 nanocrystallites by epoxy-functional organosilane with improved MTO catalytic performance. Microporous Mesoporous Mater 2023;360:112713. https://doi.org/10.1016/j.micromeso.2023.112713.
[28] Cordero-Lanzac T, Rodríguez-Cano MA, Palomo J, Valero-Romero MJ, Aguayo AT, Bilbao J, et al. Binderless ZrO_2/HZSM-5 fibrillar composites by electrospinning as catalysts for the dimethyl ether-to-olefins process. Microporous Mesoporous Mater 2022;342:112102. https://doi.org/10.1016/j.micromeso.2022.112102.
[29] Statista. Ethylene demand and production capacity worldwide from 2015 to 2022 (last access: 3rd November 2022). Https://WwwStatistaCom/Statistics/1246694/Ethylene-Demand-Capacity-Forecast-Worldwide/ n.d.
[30] Statista. Propylene demand and capacity worldwide from 2015 to 2022 (last access: 3rd November 2022). Https://WwwStatistaCom/Statistics/1246689/Propylene-Demand-Capacity-Forecast-Worldwide/ n.d.
[31] Al-Dughaither AS, De Lasa H. Neat dimethyl ether conversion to olefins (DTO) over HZSM-5: Effect of SiO_2/Al_2O_3 on porosity, surface chemistry, and reactivity. Fuel 2014;138:52–64. https://doi.org/10.1016/j.fuel.2014.07.026.
[32] Pérez-Uriarte P, Ateka A, Gamero M, Aguayo AT, Bilbao J. Effect of the Operating Conditions in the Transformation of DME to olefins over a HZSM-5 Zeolite Catalyst. Ind Eng Chem Res 2016;55:6569–78. https://doi.org/10.1021/acs.iecr.6b00627.

[33] Ghavipour M, Behbahani RM, Rostami RB, Lemraski AS. Methanol/dimethyl ether to light olefins over SAPO-34: Comprehensive comparison of the products distribution and catalyst performance. J Nat Gas Sci Eng 2014;21:532–9. https://doi.org/10.1016/j.jngse.2014.09.015.

[34] Haas A, Hauber C, Kirchmann M. Time-Resolved Product Analysis of Dimethyl Ether-to-Olefins Conversion on SAPO-34. ACS Catal 2019;9:5679–91. https://doi.org/10.1021/acscatal.9b00765.

[35] Zhang S, Chen W, Yang L, Xie T, Li W, Yu D, et al. Effect of morphology and acidity control of Ni-SAPO-34 zeolite on catalytic performance of dimethyl ether to olefins. J Solid State Chem 2021;303:122503. https://doi.org/10.1016/j.jssc.2021.122503.

[36] Cui Y, Zhang Q, He J, Wang Y, Wei F. Pore-structure-mediated hierarchical SAPO-34: Facile synthesis, tunable nanostructure, and catalysis applications for the conversion of dimethyl ether into olefins. Particuology 2013;11:468–74. https://doi.org/10.1016/j.partic.2012.12.009.

[37] Lee SG, Kim HS, Kim YH, Kang EJ, Lee DH, Park CS. Dimethyl ether conversion to light olefins over the SAPO-34/ZrO_2 composite catalysts with high lifetime. J Ind Eng Chem 2014;20:61–7. https://doi.org/10.1016/j.jiec.2013.04.026.

[38] Gao Y, Chen SL, Wei Y, Wang Y, Sun W, Cao Y, et al. Kinetics of coke formation in the dimethyl ether-to-olefins process over SAPO-34 catalyst. Chem Eng J 2017;326:528–39. https://doi.org/10.1016/j.cej.2017.05.158.

[39] Zhao D, Zhang Y, Li Z, Wang Y, Yu J. Synthesis of AEI/CHA intergrowth zeolites by dual templates and their catalytic performance for dimethyl ether to olefins. Chem Eng J 2017;323:295–303. https://doi.org/10.1016/j.cej.2017.04.109.

[40] Zhao D, Zhang Y, Li Z, Wang Y, Yu J. Synthesis of SAPO-18/34 intergrowth zeolites and their enhanced stability for dimethyl ether to olefins. RSC Adv 2017;7:939–46. https://doi.org/10.1039/c6ra25080g.

[41] Zhang Y, Ding H, Li L, Zhu K, Liu J. Generating nanocrystalline SAPO-34 through bead-milling and porogen-assisted recrystallization: Structural evolution and catalytic consequence in dimethyl ether-to-olefin conversion. Appl Catal A Gen 2022;632:118483. https://doi.org/10.1016/j.apcata.2022.118483.

[42] Cordero-Lanzac T, Ateka A, Pérez-Uriarte P, Castaño P, Aguayo AT, Bilbao J. Insight into the Deactivation and Regeneration of HZSM-5 Zeolite Catalysts in the Conversion of Dimethyl Ether to Olefins. Ind Eng Chem Res 2018;57:13689–702. https://doi.org/10.1021/acs.iecr.8b03308.

[43] Omojola T, Lukyanov DB, van Veen AC. Transient kinetic studies and microkinetic modeling of primary olefin formation from dimethyl ether over ZSM-5 catalysts. Int J Chem Kinet 2019;51:528–37. https://doi.org/10.1002/kin.21275.

[44] Omojola T, van Veen AC. Mechanistic insights into the conversion of dimethyl ether over ZSM-5 catalysts: A combined temperature-programmed surface reaction and microkinetic modelling study. Chem Eng Sci 2021;239:116620. https://doi.org/10.1016/j.ces.2021.116620.

[45] Pérez-Uriarte P, Ateka A, Aguayo AT, Bilbao J. Comparison of HZSM-5 Zeolite and SAPO (-18 and -34) Based Catalysts for the Production of Light Olefins from DME. Catal Letters 2016;146:1892–902. https://doi.org/10.1007/s10562-016-1829-z.

[46] Pérez-Uriarte P, Gamero M, Ateka A, Díaz M, Aguayo AT, Bilbao J. Effect of the Acidity of HZSM-5 Zeolite and the Binder in the DME Transformation to Olefins. Ind Eng Chem Res 2016;55:1513–21. https://doi.org/10.1021/acs.iecr.5b04477.

[47] Pérez-Uriarte P, Ateka A, Aguayo AT, Gayubo AG, Bilbao J. Kinetic model for the reaction of DME to olefins over a HZSM-5 zeolite catalyst. Chem Eng J 2016;302:801–10. https://doi.org/10.1016/j.cej.2016.05.096.

[48] Pérez-Uriarte P, Ateka A, Gayubo AG, Cordero-Lanzac T, Aguayo AT, Bilbao J. Deactivation kinetics for the conversion of dimethyl ether to olefins over a HZSM-5 zeolite catalyst. Chem Eng J 2017;311:367–77. https://doi.org/10.1016/j.cej.2016.11.104.

[49] Chen Z, Li Z, Zhang Y, Chevella D, Li G, Chen Y, et al. A green route for the synthesis of nano-sized hierarchical ZSM-5 zeolite with excellent DTO catalytic performance. Chem Eng J 2020;388:124322. https://doi.org/10.1016/j.cej.2020.124322.

[50] Bakare IA, Muraza O, Sanhoob MA, Miyake K, Hirota Y, Yamani ZH, et al. Dimethyl ether-to-olefins over aluminum rich ZSM-5: The role of Ca and La as modifiers. Fuel 2018;211:18–26. https://doi.org/10.1016/j.fuel.2017.08.117.

[51] Kolesnichenko N v., Khivrich N, Obukhova TK, Batova I, Bondarenko GN. Effect of magnesium on the catalytic properties of polymetallic zeolite catalysts for conversion of dimethyl ether to light olefins. Microporous and Mesoporous Materials 2020;298:110087. https://doi.org/10.1016/j.micromeso.2020.110087.

[52] Galanova EG, Magomedova MV, Afokin MI, Starozhitskaya AV, Maximov AL. Synthesis of olefins from dimethyl ether in a synthesis gas atmosphere. Catal Commun 2021;153:106297. https://doi.org/10.1016/j.catcom.2021.106297.

[53] Park S, Watanabe Y, Nishita Y, Fukuoka T, Inagaki S, Kubota Y. Catalytic conversion of dimethyl ether into propylene over MCM-68 zeolite. J Catal 2014;319:265–73. https://doi.org/10.1016/j.jcat.2014.09.002.

[54] Nasser G, Kurniawan T, Miyake K, Galadima A, Hirota Y, Nishiyama N, et al. Dimethyl ether to olefins over dealuminated mordenite (MOR) zeolites derived from natural minerals. J Nat Gas Sci Eng 2016;28:566–71. https://doi.org/10.1016/j.jngse.2015.12.032.

[55] Kurniawan T, Muraza O, Miyake K, Hakeem AS, Hirota Y, Al-Amer AM, et al. Conversion of Dimethyl Ether to Olefins over Nanosized Mordenite Fabricated by a Combined High-Energy Ball Milling with Recrystallization. Ind Eng Chem Res 2017;56:4258–66. https://doi.org/10.1021/acs.iecr.6b04834.

[56] Ahmed MHM, Muraza O, al Amer AM, Sugiura Y, Nishiyama N. Development of desilicated EU-1 zeolite and its application in conversion of dimethyl ether to olefins. Microporous and Mesoporous Materials 2015;207:9–16. https://doi.org/10.1016/j.micromeso.2015.01.006.

[57] Ahmed MHM, Muraza O, Al-Amer AM, Miyake K, Nishiyama N. Development of hierarchical EU-1 zeolite by sequential alkaline and acid treatments for selective dimethyl ether to propylene (DTP). Appl Catal A Gen 2015;497:127–34. https://doi.org/10.1016/j.apcata.2015.03.011.

[58] Ahmed MHM, Muraza O, Miyake K, Hirota Y, Nishiyama N. Orchestrating fluoride effect, secondary growth and microwave irradiation in the synthesis of EU-1/ZSM-48 intergrowth crystals for the conversion of dimethyl ether to olefins. Microporous Mesoporous Mater 2018;267:115–23. https://doi.org/10.1016/j.micromeso.2018.02.047.

[59] Frusteri F, Bonura G, Cannilla C, Drago Ferrante G, Aloise A, Catizzone E, et al. Stepwise tuning of metal-oxide and acid sites of CuZnZr-MFI hybrid catalysts for the direct DME synthesis by CO_2 hydrogenation. Appl Catal B 2015;176–177:522–31. https://doi.org/10.1016/j.apcatb.2015.04.032.

[60] Ferrarelli G, Giordano G, Migliori M. ZSM-5@Sil-1 core shell: Effect of synthesis method over textural and catalytic properties. Catal Today 2022;390–391:176–84. https://doi.org/10.1016/j.cattod.2021.11.036.

[61] Miletto I, Catizzone E, Bonura G, Ivaldi C, Migliori M, Gianotti E, et al. In situ FT-IR characterization of CuZnZr/ferrierite hybrid catalysts for one-pot CO_2-to-DME conversion. Materials 2018;11. https://doi.org/10.3390/ma11112275.

[62] Scanlon JT, Willis DE. Calculation of Flame Ionization Detector Relative Response Factors Using the Effective Carbon Number Concept. J Chromatogr Sci 1985;23:333–40. https://doi.org/10.1093/chromsci/23.8.333.

[63] Giordano G, Migliori M, Ferrarelli G, Giorgianni G, Dalena F, Peng P, et al. Passivated Surface of High Aluminum Containing ZSM-5 by Silicalite-1: Synthesis and Application in Dehydration Reaction. ACS Sustain Chem Eng 2022;10:4839–48. https://doi.org/10.1021/acssuschemeng.1c07198.

[64] Jin Z, Liu S, Qin L, Liu Z, Wang Y, Xie Z, et al. Methane dehydroaromatization by Mo-supported MFI-type zeolite with core-shell structure. Appl Catal A Gen 2013;453:295–301. https://doi.org/10.1016/j.apcata.2012.12.043.

[65] Catizzone E, Aloise A, Giglio E, Ferrarelli G, Bianco M, Migliori M, et al. MFI vs. FER zeolite during methanol dehydration to dimethyl ether: The crystal size plays a key role. Catal Commun 2021;149:106214. https://doi.org/10.1016/j.catcom.2020.106214.

[66] Catizzone E, Ferrarelli G, Bruno P, Giordano G, Migliori M. Simultaneous catalytic dehydration of methanol and ethanol: How ZSM-5 acidity addresses conversion and products distribution. Catal Today 2024;427. https://doi.org/10.1016/j.cattod.2023.114436.

[67] Armaroli T, Trombetta M, Gutièrrez Alejandre A, Solis JR, Busca G. FTIR study of the interaction of some branched aliphatic molecules with the external and internal sites of H-ZSM5 zeolite. PCCP 2000;2:3341–8. https://doi.org/10.1039/b001807o.

[68] Catizzone E, Aloise A, Migliori M, Giordano G. From 1-D to 3-D zeolite structures: performance assessment in catalysis of vapour-phase methanol dehydration to DME. Microporous Mesoporous Mater 2017;243:102–11. https://doi.org/10.1016/j.micromeso.2017.02.022.

[69] Catizzone E, Aloise A, Migliori M, Giordano G. Dimethyl ether synthesis via methanol dehydration: Effect of zeolite structure. Appl Catal A Gen 2015;502:215–20. https://doi.org/10.1016/j.apcata.2015.06.017.

[70] Catizzone E, Giglio E, Migliori M, Cozzucoli PC, Giordano G. The Effect of Zeolite Features on the Dehydration Reaction of Methanol to Dimethyl Ether: Catalytic Behaviour and Kinetics. Materials 2020;13:5577. https://doi.org/10.3390/ma13235577.

[71] Tian P, Wei Y, Ye M, Liu Z. Methanol to olefins (MTO): From fundamentals to commercialization. ACS Catal 2015. https://doi.org/10.1021/acscatal.5b00007.

[72] Bjørgen M, Svelle S, Joensen F, Nerlov J, Kolboe S, Bonino F, et al. Conversion of methanol to hydrocarbons over zeolite H-ZSM-5: On the origin of the olefinic species. J Catal 2007;249:195–207. https://doi.org/10.1016/j.jcat.2007.04.006.

[73] Ilias S, Bhan A. Mechanism of the Catalytic Conversion of Methanol to Hydrocarbons. ACS Catal 2013;3:18–31. https://doi.org/10.1021/cs3006583.